

Uncertainty quantification in a heterogeneous fluvial sandstone reservoir using GPU-based Monte Carlo simulation

Yang Wang ^{a,c}, Denis Voskov ^{a,b,*}, Alexandros Daniilidis ^a, Mark Khait ^{a,d}, Sanaz Saeid ^a, David Bruhn ^{a,e}

^a Faculty of Civil Engineering and Geosciences, Delft University of Technology, The Netherlands

^b Department of Energy Resources Engineering, Stanford University, USA

^c Department of Civil Engineering, Qingdao University of Technology, China

^d Stone Ridge Technology S.R.L., Milan, Italy

^e Competence Centre Global Georesources, Fraunhofer IEG, Germany

ARTICLE INFO

Keywords:
Geothermal uncertainty quantification
Monte Carlo simulation
GPU platform
Net present value
Energy production

ABSTRACT

The efficient operation and management of a geothermal project can be largely affected by geological, physical, operational and economic uncertainties. Systematic uncertainty quantification (UQ) involving these parameters helps to determine the probability of the focused outputs, e.g., energy production, Net Present Value (NPV), etc. However, how to efficiently assess the specific impacts of different uncertain parameters on the outputs of a geothermal project is still not clear. In this study, we performed a comprehensive UQ to a low-enthalpy geothermal reservoir using the GPU implementation of the Delft Advanced Research Terra Simulator (DARTS) framework with stochastic Monte Carlo samplings of uncertain parameters. With processing the simulation results, large uncertainties have been found in the production temperature, pressure drop, produced energy and NPV. It is also clear from the analysis that salinity influences the producing energy and NPV via changing the amount of energy carried in the fluid. Our work shows that the uncertainty in NPV is much larger than that in produced energy, as more uncertain factors were encompassed in NPV evaluation. An attempt to substitute original 3D models with upscaled 2D models in UQ demonstrates significant differences in the stochastic response of these two approaches in representation of realistic heterogeneity. The GPU version of DARTS significantly improved the simulation performance, which guarantees the full set (10,000 times) UQ with a large model (circa 3.2 million cells) finished within a day. With this study, the importance of UQ to geothermal field development is comprehensively addressed. This work provides a framework for assessing the impacts of uncertain parameters on the concerning system output of a geothermal project and will facilitate analyses with similar procedures.

1. Introduction

With the intensified global warming phenomenon, people endeavor to mitigate the greenhouse gas (or say, CO₂) emission through cooperation between governments, like the assignment of the Paris Agreement, and the large-scale utilization of renewable energy, such as geothermal and wind energy. The management of energy applications related to subsurface resources should consider the uncertain parameters sufficiently (Bickel and Bratvold, 2008). The developing strategies of subsurface systems can be adjusted after consideration of uncertainties, which have been shown in various industrial applications (James and Oldenburg, 1997; Ballio and Guadagnini, 2004; Scheidt and Caers, 2009; Dai et al., 2014). Without exceptions, the energy production

from geothermal reservoirs can be easily perturbed by uncertainties as well (Shetty et al., 2018; Saeid et al., 2020).

The uncertainties in geothermal production can come from various aspects. First, limited by geological measurements and samples, our knowledge about a target reservoir is generally based on data interpretation and empirical correlations. For example, the relationship between permeability and porosity is often based on empirical petrophysical correlations (Willems et al., 2020), while the porosity values are often interpreted from core analysis and log curves (Chang et al., 1994). However, the spatial distribution of permeability and porosity is highly uncertain (Major et al., 2023). Besides, the physical and thermal properties of fluids (e.g., salinity, density) and rock (e.g., thermal

* Corresponding author at: Faculty of Civil Engineering and Geosciences, Delft University of Technology, The Netherlands.
E-mail address: D.V.Voskov@tudelft.nl (D. Voskov).

capacity and conductivity) can vary with mineral dissolution and rock compositions at geological time scales. These variations impact the amount of energy and heat transport processes inside the reservoir. Furthermore, the operations of a geothermal reservoir should take the economic part into account, which directly determines the project benefit (Daniilidis et al., 2021). Nevertheless, the economic parameters (e.g., heat and electricity prices) will fluctuate with the markets, which introduces uncertainties in the comprehensive appraisal of a geothermal project (De Paepe and Mertens, 2007).

Quantifying the influence of uncertain key parameters in advance will assist reservoir management and improve the developing schemes in time. Numerical simulation, as an effective tool, can be utilized to inspect the reservoir's response to the presence of various uncertainties during development (Xu et al., 2007; Jansen et al., 2009). Large numerical models could be constructed to fully capture the reservoir heterogeneity in the subsurface geology. Therefore, the uncertainties of geological information can be easily characterized within different numerical models. In the meanwhile, the uncertainty analysis of geothermal production can connect with Monte Carlo (MC) simulation, which has been widely used to quantify the uncertainties in subsurface applications with ensembles of forward models (Ballio and Guadagnini, 2004; Cremon et al., 2020). MC performs simulations with input data sampled stochastically within a given distribution in the parameter space. How representative are the MC results depends on the dimension of the uncertain parameter space and the nonlinearity of the underlying model. To achieve converging results, MC usually has to perform a large number of forward simulations, which requires a high-performance numerical simulation framework and abundant computation resources, especially for large models with detailed geological characterization (Athens and Caers, 2019).

A popular treatment to mitigate the computational challenges for larger models is property upscaling. Besides running on more advanced computing hardware or with advanced computational methods, the simulation models are often compromised with coarse resolutions by efficient upscaling-based approaches. Several classical upscaling methods (Chen et al., 2003; Chen and Durlofsky, 2006; Gong et al., 2008) were proposed for isothermal reservoir simulations, in which the model resolution is allowed to be upscaled from the fine geological resolution to different levels of coarse resolutions. In most uncertainty and sensitivity studies, the fully heterogeneous 3D model is often upscaled or simplified to a 2D model to accommodate the limited computational performance of the simulator (Veldkamp et al., 2015). With an upscaled model, the reservoir numerical simulation will certainly accelerate. However, the model resolution affects both the performance and accuracy of the simulations. In geothermal systems, heat transport is governed by the complex interplay of thermal convection and conduction (Wang et al., 2021; Daniilidis et al., 2021). The generally-ignored or coarsely-upscaled entities (e.g., shale facies) in isothermal simulation should be carefully dealt with in geothermal systems (Wang et al., 2021). To the best of our knowledge, it keeps an open question of how to effectively upscale the non-reservoir lithologies in geothermal simulations (Perkins, 2019). Consequently, the demanding computational workload of large models (e.g., with millions of grid blocks) remains challenging for conventional reservoir simulators.

With the development of GPU computing architecture, high-performance computation reduces the time required for laborious simulations to an affordable time. In our study, a general-purpose numerical simulator called Delft Advanced Research Terra Simulator (**DARTS**, 2023), is utilized to perform geothermal modeling. DARTS is constructed within the advanced Operator-Base Linearization (OBL) technique (Voskov, 2017). Both efficiency and accuracy of DARTS for geothermal simulation have been benchmarked against state-of-the-art simulation frameworks (Wang et al., 2020). The recent implementation of GPU and multithread CPU versions of DARTS (Khait and Voskov, 2017; Khait et al., 2020) have largely improved the simulation performance. A benchmark study (Khait et al., 2020) demonstrates

the geothermal simulation with DARTS on GPU achieves an order of magnitude faster speed than a single thread CPU simulation.

In this study, systematic uncertainty quantification (UQ) is performed for a geothermal reservoir with detailed reservoir characterizations, which capture the geological heterogeneity with large, "high-cell count" models. Specifically, MC simulations with a large ensemble of models are utilized to investigate the uncertainty in produced energy and Net Present Value (NPV) with multiple input parameters, including geological data (e.g., porosity-permeability distribution), subsurface properties (e.g., salinity, rock conductivity), operational (e.g., injectivity, injection temperature) and economic parameters (e.g., heat and electricity prices). The large ensembles of forward simulations are executed on the GPU version of DARTS. Furthermore, the high-fidelity 3D models are upscaled to coarser resolutions to examine whether uncertainties exhibited in 3D models can be approximately captured by upscaled models often used for such studies. In the following content of the paper, the geological, mathematical and economic models are first introduced together with their uncertainty ranges. After a few sensitivity runs, an extensive MC convergence study is performed to examine the resulting probability density function for main geothermal characteristics. Then, a detailed uncertainty analysis is discussed based on the numerical results, followed by conclusions.

2. Models and input parameters

2.1. Geological model

The geological model is provided by a service company responsible for the geothermal field development. The study area is located in the West Netherlands Basin which is an inverted rift basin. Sediments in this basin range in age from Jurassic to Cenozoic and are overlying Triassic and older sediments. The Upper Jurassic and Lower Cretaceous start with the continental sediments of the Nieuwerkerk Formation and Vlieland sandstone Formation (Willems et al., 2020). These sediments were deposited in subsiding half-grabens, while adjacent highs were subjected to erosion (PanTerra Geoconsultants, 2018). In these formations two main reservoir layers have been observed, Berkel Sandstone and Delft Sandstone. Circa 3.2 million grid cells are used to characterize the model using a geological scale, where circa 0.8 million grid cells are for the sandstone and 2.4 million cells for shale facies.

The Berkel Sandstone Member and Berkel Sands-Claystone Member have a shallow marine depositional setting. The facies range from the upper shoreface to the lower shoreface of a coastal-barrier system. Lateral continuity is often good and cementation low. The permeability of the sands is good to excellent ranging from 400 to larger than 1000 mD. The Delft Sandstone is interpreted to be deposited as stacked distributary-channel deposits in a lower coastal plain setting resulting in massive sandstone sequences. The thickness of the Delft Sandstone is influenced by the syn-rift deposition of the sediments and therefore, the Delft Sandstone is of variable thickness; a thickness up to 130 m is observed. The sandstone consists of fine- to coarse-grained sand, and the lateral continuity is difficult to predict. Both the Berkel and Delft Sandstone are studied with wells perforated through them. Porosities range from 0.01 to 0.256 and permeabilities from 0.004 to 1308 mD (see Fig. 2).

The model extends along a horizontal direction by 9000 m × 4200 m with 177 × 85 reservoir blocks. There is a total of 895 layers along the vertical direction. Two doublets are placed in the reservoir and operated with constant rate control. Due to the fact that the boundaries are far away from the well influence area, they are assigned to no-flow boundaries. Table 1 provides some basic parameter settings of the model.

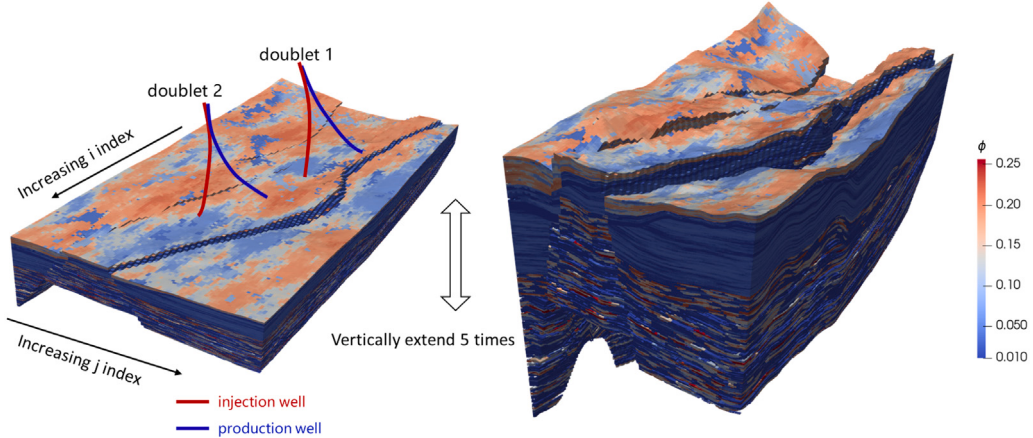


Fig. 1. Porosity distribution of the target geothermal reservoir. The model is amplified 1.5 times along the vertical direction to show the heterogeneity of the reservoir in detail. The well trajectories are connecting the following blocks in top and bottom layers respectively in the form of (i, j) indices: I1 (51, 58) - (48, 50); P1 (76, 53) - (82, 49); I2 (94, 44) - (111, 37); P2 (124, 39) - (144, 30).

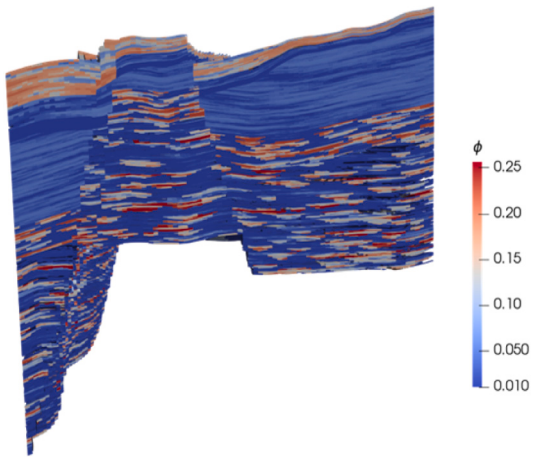


Fig. 2. Porosity distribution of the reservoir from the side view.

Table 1
Thermal and hydraulic properties of the geothermal reservoir.

Parameters	Unit	Values
Porosity	–	(0.01–0.256)
Permeability	mD	(0.004–1308)
Shale heat capacity	kJ/m ³ /K	2300
Sandstone heat capacity	kJ/m ³ /K	2450
Pressure at the top of the reservoir	bars	115
Temperature at the top of the reservoir	K	328
Thermal gradient	K/km	30
Pressure gradient	bar/km	100
Rate (doublet 1)	m ³ /s	0.0868
Rate (doublet 2)	m ³ /s	0.0868

2.2. Uncertain input parameters

The production and operation of the geothermal field can be influenced by uncertain parameters from geological, physical, operational and economic aspects. A representative selection of uncertain parameters is useful for systematic UQ. In this section, uncertain parameters from various perspectives are sampled within given distributions and will be used in the following investigation.

2.2.1. Porosity-permeability realizations

In our study, 100 realizations were generated based on a variation of the seed parameter in the base case facies model (Saeid et al., 2020).

The mean and standard deviation of parameters were kept as delivered and only the spatial distribution was varied. The facies were generated using sequential indicator simulation for the Berkel Sandstone and object modeling for the channelized Delft Sandstone. Porosities were generated by using Sequential Gaussian Simulation and permeabilities were generated using co-kriging of porosity. This limits the UQ with respect to geological parameters constrained to a proposed sedimentary scenario (see Fig. 3).

2.2.2. Salinity

Determined by the dissolved minerals and solids, the reservoir fluid can be categorized from almost fresh water to highly saline brine (Borgia et al., 2012; Kang and Jackson, 2016). Salinity has an impact on heat propagation and the production process of a geothermal system. Based on Saeid et al. (2015), the increase in salinity will result in a decrease in energy production and system lifetime for the investigated homogeneous reservoir. Since fluid samples are lacking, the specific salinity value is uncertain for the target reservoir. To account for the uncertainty of specific salinity, we selected a wide distribution of salinity values for our analysis, conforming to the normal distribution (mean $\mu = 0.125 \text{ ppm}/1\text{e}6$ with standard deviation $\sigma = 0.050 \text{ ppm}/1\text{e}6$ Fig. 4).

According to Batzle and Wang (1992), the brine density as a function of salinity, temperature and pressure is described as,

$$\rho_s = \rho_w + S [0.668 + 0.44S + 1e^{-6} (300P - 2400PS + T(80 + 3T - 3300S - 13P + 47PS))] \quad (1)$$

The brine viscosity as a function of salinity and temperature is described as,

$$\mu_s = 0.1 + 0.333S + (1.65 + 91.9S^3) \exp [-(0.42(S^{0.8} - 0.17)^2 + 0.045)T^{0.8}], \quad (2)$$

where ρ_s and ρ_w are saline and water density [kg/m^3], μ_s is viscosity [mPa s], S is the brine mass fraction [$\text{ppm}/10^6$], P is the pressure [MPa] and T is temperature [$^\circ\text{C}$]. In the uncertainty quantification study, we assume that both density and viscosity are dependent on a single salinity value randomly sampled.

2.2.3. Rock thermal conductivity

The thermal conductivity of the rock determines the speed of heat exchange when a temperature gradient is present. The importance of thermal conduction of different types of rocks for heat production and propagation in geothermal systems has been studied and stressed (Daniilidis and Herber, 2017; Wang et al., 2021). However, the sensitivity

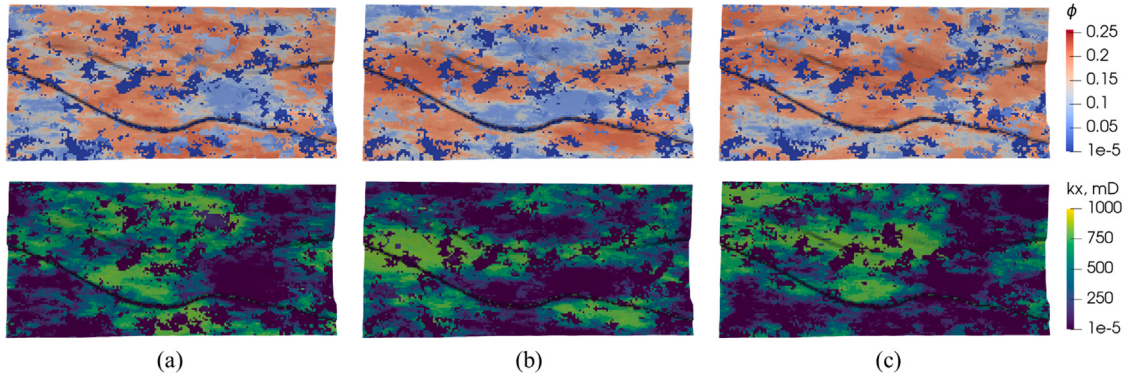


Fig. 3. Top view of the porosity and permeability distribution of three model realizations. The first row represents the porosity distribution, while the second row represents the corresponding permeability distribution.

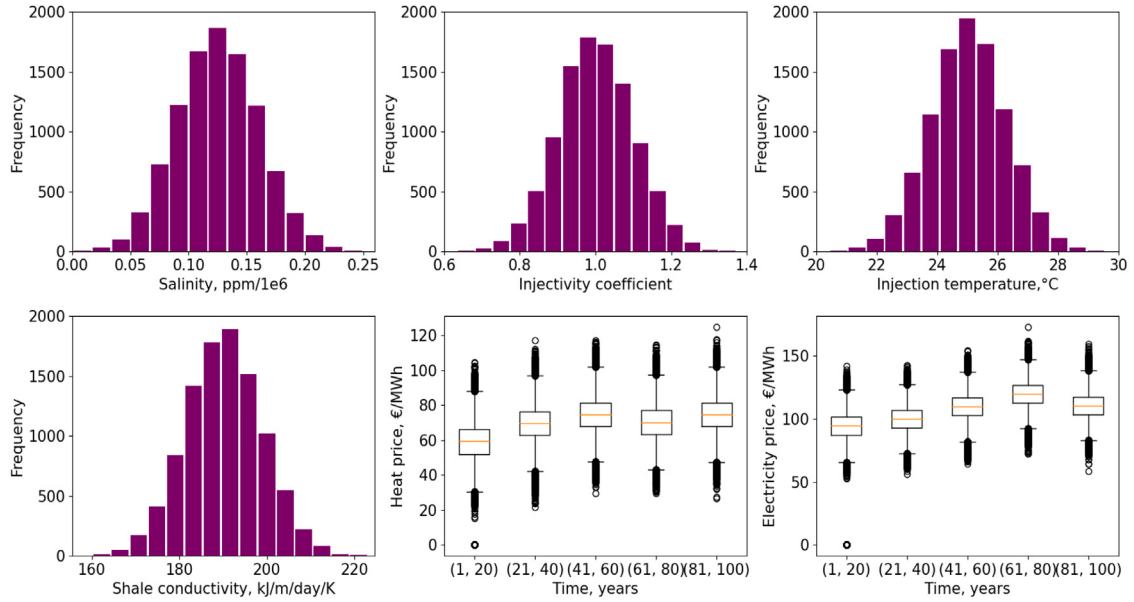


Fig. 4. The histograms and distributions of the uncertain input parameters.

of energy production to the magnitude of rock conductivity has not been studied before. It can be measured in the laboratory under in-situ conditions. It varies with several factors, for example, the mineral composition of the rock, the presence of fluids, pressure, etc (Labus and Labus, 2018). Heat production should consider the introduced uncertainties in rock conductivity by these factors. The target reservoir in this study consists of two types of rocks, shale and sandstone, both of which are sedimentary rocks. The thermal conductivities of shale and sandstone (Fig. 4) are assumed to follow a normal distribution. Typical numbers were selected (MidtØmme and Roaldset, 1999; Labus and Labus, 2018) for shale (mean $\mu = 190.08 \text{ kJ/m/day/K}$, standard deviation $\sigma = 8.64 \text{ kJ/m/day/K}$) and sandstone (mean $\mu = 259.2 \text{ kJ/m/day/K}$, standard deviation $\sigma = 8.64 \text{ kJ/m/day/K}$).

2.2.4. Injection temperature

Energy production is subject to the injection temperature, which will impact the lifetime of a geothermal reservoir (Saeid et al., 2015; Aliyu and Chen, 2017; Zaal et al., 2021). The magnitude of the injection temperature can vary with heat exchange and heat losses during energy utilization and transportation. Therefore, the injection temperature is expected to fluctuate a bit around certain values. A normal distribution (mean $\mu = 25^\circ\text{C}$, standard deviation $\sigma = 1.5^\circ\text{C}$ Fig. 4) was assumed to describe the uncertainty existing in the injection temperature.

2.2.5. Well injectivity

The re-injection of cold water into the reservoir will initiate mineral precipitation or thermal cracking (Benson et al., 1987) in the near-wellbore region. The injectivity of a geothermal doublet will be reduced or enhanced correspondingly. In the numerical simulation, the well index following the Peaceman (1983) equation is used to characterize the well injectivity

$$WI = \frac{2\pi \sqrt{k_x k_y} h}{\ln(r_w/r_o)}. \quad (3)$$

Here, based on the default evaluation of well index, an additional injectivity coefficient was randomly sampled from a normal distribution (mean $\mu = 1$, standard deviation $\sigma = 0.1$ Fig. 4). During one MC simulation, the sampled coefficient was multiplied by the default well index to represent the uncertainty of well injectivity. In this study, since both doublets operate at a constant rate, the well injectivity will influence the pressure drop between injector and producer wells within each doublet. Therefore, the required pumping energy will be different.

2.2.6. Economics

Varying on the energy source and providers, the heat and electricity prices will fluctuate within the studied period (De Paepe and Mertens, 2007). To more accurately examine the uncertain impact of heat and electricity prices on NPV, the 100-years simulation time was divided

Table 2

Parameters utilized in NPV calculation.

Parameters	Unit	Values
Pump cost	k€	500
Pump lifetime	years	5
Pump efficiency	%	60
OpEx (% of CapEx/year)	%	5
Discount rate	%	10

into 20-year sub-intervals. Within each sub-interval, it was assumed the prices fluctuate around a mean value within a normal distribution. The prices of each year within this interval were sampled from the normal distribution. The distribution of heat and electricity prices is shown in Fig. 4. The relevant parameters for NPV calculation are listed in Table 2. Capital Expenses (CapEx) are discrete investments; these include the costs for the exploration phase, the drilling of the wells, the construction costs for the heat network and drilling facilities, equipment (heat exchanger, gas separator) and the recurring costs for the electrical submersible pump. The Operational Expenses (OpEx) are computed as a percentage of the CapEx with the pump power electricity added (Daniilidis et al., 2017).

2.3. Numerical model

The general mass and energy conservation equations are taken to model the dynamic flow and transport processes during the field development. In low-enthalpy geothermal reservoirs, the brackish to highly saline brine is often encountered as working fluids with some chemical additives. Without loss of generality, the saline brine is chosen as the heat carrier here.

$$\frac{\partial}{\partial t}(\phi\rho_f) - \nabla \cdot (\rho_f u_f) + \rho_f \tilde{q}_f = 0, \quad (4)$$

$$\frac{\partial}{\partial t}(\phi U_f + (1-\phi)U_r) - \nabla \cdot (h_f \rho_f u_f) + \nabla \cdot (\kappa \nabla T) + h_f \rho_f \tilde{q}_f = 0, \quad (5)$$

where Eq. (4) is the mass conservation equation and Eq. (5) is the energy conservation equation. Here ϕ is the porosity, ρ_f is the fluid density [kg/m^3], u_f is the fluid flow velocity [m/s], \tilde{q}_f is the fluid source/sink term per volume [$1/\text{s}$], U_f is the fluid internal energy [kJ/m^3], U_r is the rock internal energy [kJ/m^3], h_f is the fluid enthalpy [kJ/kg], κ is the thermal conductivity [$\text{kJ}/\text{m}/\text{day}/\text{K}$].

The different quantities in Eqs. (4)–(5) are defined as follows. The fluid internal energy per volume is expressed as:

$$U_f = \rho_f h_f - p_f, \quad (6)$$

where p_f is the fluid pressure [bars] and the rock internal energy per volume is expressed as:

$$U_r = C_r(T - T_{\text{ref}}), \quad (7)$$

where C_r is the volumetric heat capacity of rock [$\text{kJ}/\text{m}^3/\text{K}$], T_{ref} is the reference temperature [K]. The rock is compressible, which is reflected by the change of porosity through:

$$\phi = \phi_0(1 + c_r(p_f - p_{\text{ref}})), \quad (8)$$

where ϕ_0 is the initial porosity, c_r is the rock compressibility [$1/\text{bars}$] and p_{ref} is the reference pressure [bars]. The fluid is also compressible and its properties are evaluated through IAPWS-97 (Kretzschmar and Wagner, 2007). In addition, Darcy's law is used to describe the fluid flow in the reservoir,

$$u_f = -\frac{K}{\mu_f}(\nabla p_f - \gamma \nabla D), \quad (9)$$

where: K is the permeability [mD], μ_f is the fluid viscosity [mPa s], γ is the fluid specific weight [N/m^3], D is the depth [m].

The governing equation systems are solved in a fully-coupled way in DARTS, where a general unstructured finite volume mesh discretization is combined with a backward Euler approximation in time. The advanced Operator-Based Linearization (OBL) approach (Voskov, 2017) is deployed within DARTS to discretize the physical space, which highly improves the simulation efficiency with enough accuracy (Khait and Voskov, 2018). A detailed description and applications of DARTS are available on the project website (DARTS, 2023).

2.4. Economic model

To perform an economic analysis, we take the model from Daniilidis et al. (2021). The power [W] produced from the well is computed according to

$$P_{\text{well}} = Q \rho_f h_f, \quad (10)$$

in which Q is the flow rate [m^3/s]. The required pump power [W] only considers the pressure drop in the reservoir,

$$P_{\text{pump}} = \frac{\Delta p Q}{\eta}, \quad (11)$$

where Δp is the pressure difference between the injection and production wells [Pa], η is the pump efficiency. The total system power is evaluated as

$$P_{\text{system}} = P_{\text{prod}} - P_{\text{inj}} - P_{\text{pump}}. \quad (12)$$

The cumulative energy produced from the system is computed using

$$E_{\text{cum}} = \sum_{t=0}^n P_{\text{well}_t}, \quad (13)$$

where n is the project time, t is the specific year. The cost of drilling the well is computed according to TNO (2018),

$$C_{\text{well}} = 375000 + 1150Z + 0.3Z^2, \quad (14)$$

where Z is the measured depth along the wellbore. The NPV is calculated as Daniilidis et al. (2017),

$$NPV = \sum_{t=0}^n \frac{CF_t}{(1+r)^t}, \quad (15)$$

where CF is the cash flow on a yearly basis, r is the periodic discount rate and t is the time period. Cash flow simply means the difference between income and cost during a certain period of time. The cumulative produced power generates income based on the heat price, while the pump power costs are computed based on the electricity price. The combined system energy is the summation of the two doublets. The aggregated results are then used for the NPV calculations, over yearly intervals.

3. Convergence analysis of MC simulations

Though it is difficult to set general criteria to calibrate the convergence of MC simulations, the results are expected to reach statistical convergence when the amount of samples is large enough (Ballio and Guadagnini, 2004). The convergence rate may vary with the studied problem and variables. Convergence is assumed to be reached if the distribution stays stable with increasing the number of MC realizations. Here, L_2 norm is utilized to quantitatively characterize the convergence of distributions. L_2 norm is defined by $\|X_n - X_{n-1}\|_2$, where X_n and X_{n-1} are the normalized distribution at current and previous computation steps.

In this study, in total 10,000 MC simulations were performed. Energy production and NPV are taken as two of the most concerning parameters. Fig. 5 shows L_2 norm of the difference between energy and NPV distributions in the MC simulation process. As expected, the distribution difference drops with the increase of MC samplings. With

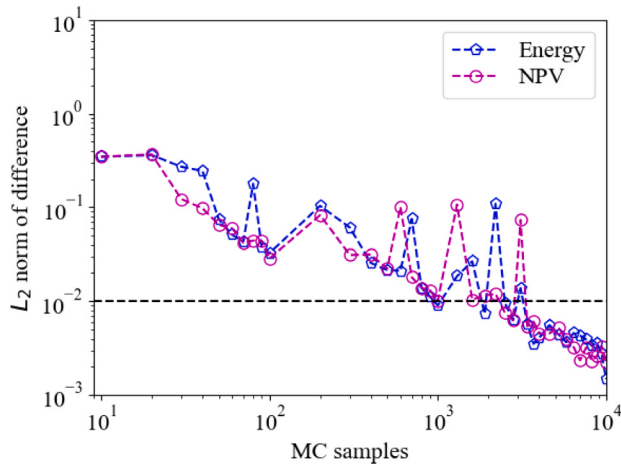


Fig. 5. L_2 norm of the distribution difference with the increase of MC samples for produced energy and NPV.

approximately 3000 realizations, the distribution difference becomes smaller than 1%, which is regarded as converged MC simulations.

To make a further check about the convergence of the MC simulations, the quantiles of the energy production and NPV of the 10,000 simulations were compared. Figs. 6 and 7 display the P10, P50 and P90 of the produced energy and NPV with an increasing number of MC samples. Fig. 6(a) shows an example of MC simulation convergence of P10. Based on the daily energy production rate, the total energy production of each MC sample can be evaluated at the end of the simulation. The energy production of all realizations is then collected as a data set. With an increasing number of MC samples, the 10% probability of the counted data was sequentially calculated, which in the end generated one curve in Fig. 6(a). The data set was then randomly shuffled and the 10% probability is re-evaluated correspondingly multiple times. Fig. 6(a) is made up of all these evaluations, with a similar procedure followed for plots in Fig. 6 and Fig. 7. Wide spreading of produced energy and NPV is noticed while the number of realizations is limited. To get representative values of produced energy and NPV, a minimum of 3000 realizations are required in our study to converge MC simulations for a given quantile. The P10, P50 and P90 values of the total produced energy in our study are 149, 144 and 140 PJ respectively, while the P10, P50 and P90 values of total NPV are 109, 99 and 88 M€ respectively.

4. Numerical results and analyses

4.1. Production temperature and pressure drop

Fig. 8 displays the production temperature of all realizations for both doublets. For doublet 1, the temperature starts to drop at around the 20th year for the ensemble of models, while it is at around 10th year for doublet 2. A maximum temperature difference of 6 K at 100 years of operation for doublet 1 is observed. The production temperature of doublet 1 is largely impacted by uncertain parameters. A temperature of 323.5 K (P50) has the highest probability at the end of the simulation. In addition, the overall temperature drop for doublet 2 (9 degrees) is less than for doublet 1 (12 degrees), which is an indication of well interference. The well interference suggests that there is a diversion effect of doublet 1 to the injection well of doublet 2, which influences the thermal propagation of doublet 2. As is shown in Fig. 1, the injection well of doublet 2 is close to the producer of doublet 1, which indicates the water supply of doublet 2 to doublet 1. Therefore, the cold front propagation becomes a bit slower in the controlled area of doublet 2.

Fig. 9 shows the pressure drop between Bottom Hole Pressure (BHP) of all realizations for both doublets. The pressure drop of doublet 1 after 100 years ranges from 50 bars to 100 bars (Fig. 9(a)), where a 70-bar drop represents the P50 value. The pressure drop of doublet 2 varies from 35 bars to 115 bars (Fig. 9(b)), where 50-bars is the most probable pressure drop (P50). This shows that the uncertain parameters have a stronger impact on the pressure calculation for doublet 2. In addition, the magnitude of pressure drop calculated for doublet 1 is, on average, larger than for doublet 2. This indicates that the average flow resistance is smaller within the controlled area of doublet 1, as the distance between the two wells in both doublets is similar Fig. 1.

4.2. Energy, NPV and break-even time

Fig. 10 displays the distribution of the cumulative produced energy and NPV of all realizations at the end of the simulations. Both the energy and NPV follow a normal distribution. Since the input parameters are sampled with normal distributions (except the randomly sampled poro-perm realizations), the observed system response to the combined input seems predictable, although the individual impact of each input parameter can be different, as discussed below. However, for complex subsurface systems like in this study, the outputs from ensemble models will be highly case-dependent, which is difficult to predict without systematic forward simulations. Assumptions made in this study, such as the fixed production rate of each doublet, reduce the variability of the final results and the uncertainty in the model outputs.

The difference in energy production between P10 and P90 is 9 PJ, while the spread of NPV between P10 and P90 is 21 M€. To quantify the uncertainties, we define an uncertain factor (α) as the ratio of (P10, P90) difference and P50 value, $\alpha = \frac{(X_{P10} - X_{P90})}{(X_{P50})} \times 100\%$. With this definition, the uncertainty of NPV (21.21%) is larger than that of produced energy (6.25%). On the one hand, it is because two additional uncertain input parameters (heat and electricity price) are considered in the NPV evaluation. On the other hand, the NPV calculation takes more factors (e.g., pressure drop within a doublet, injected energy, etc.) into account, which will be discussed in the following section. As a comparison, the produced energy delivers a more straightforward message about the uncertainty of heat transport and thermal exchange inside the reservoir.

Fig. 11 displays the cumulative NPV of all realizations and the converged break-even time. As is shown in Fig. 11(a), a large cash investment is required at the beginning of the project, including drilling and equipment costs. Based on a 10% discount rate, the NPV already experiences decelerated growth at the end of the 30th year and reaches a plateau within the last 50 years of production.

Break-even time refers to the amount of time required for the discounted cash flows generated by a project to equal its initial cost (NPV = 0). With the selected production strategy, a break-even time of less than 2 years is expected. This project will become net profitable after 2 years and there are no risk factors foreseeable with the uncertainty of the parameters considered in this study.

4.3. Uncertainty of system outputs to individual parameters

The output uncertainty to aggregated input parameters has been discussed in the previous parts. This section will show the influence of individual uncertain parameters on produced energy and NPV under the presence of other uncertain parameters. In Fig. 12, the independent impact of six parameters (poro-perm realization, salinity, injectivity coefficient, injection temperature, shale and sandstone conductivity) on total energy production is listed. In each subplot, values of the investigated parameter are first divided into sub-intervals, which are used as filters for the MC samples. The energy distribution of the filtered MC samples is then plotted against each sub-interval correspondingly. The sensitivity of energy to different parameters can be observed within these plots.

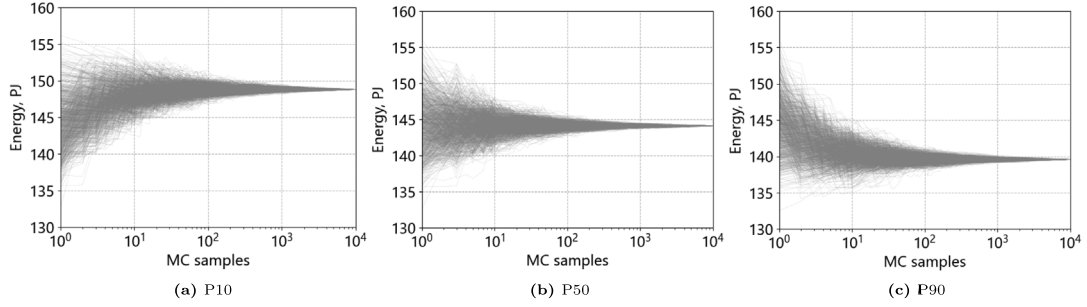


Fig. 6. The asymptotic tendency of P10, P50 and P90 quantiles of the cumulative energy production of 100 years.

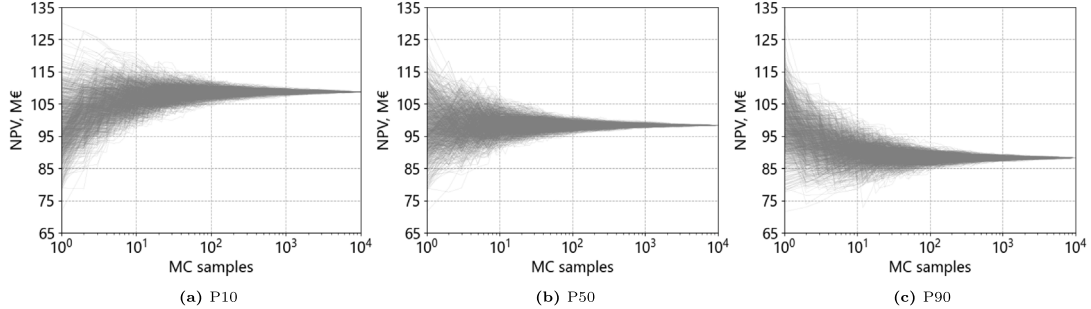


Fig. 7. The asymptotic tendency of P10, P50 and P90 quantiles of the NPV of 100 years.

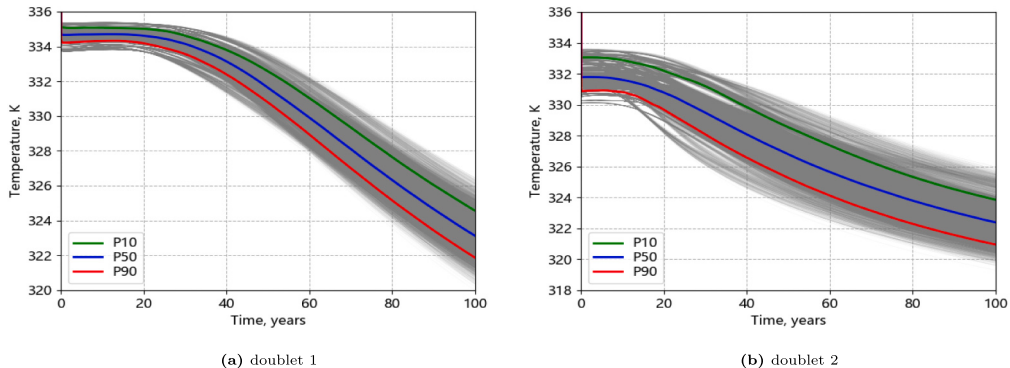


Fig. 8. Production temperature of doublet 1 and 2, and the corresponding P10, P50, P90 production temperature curves.

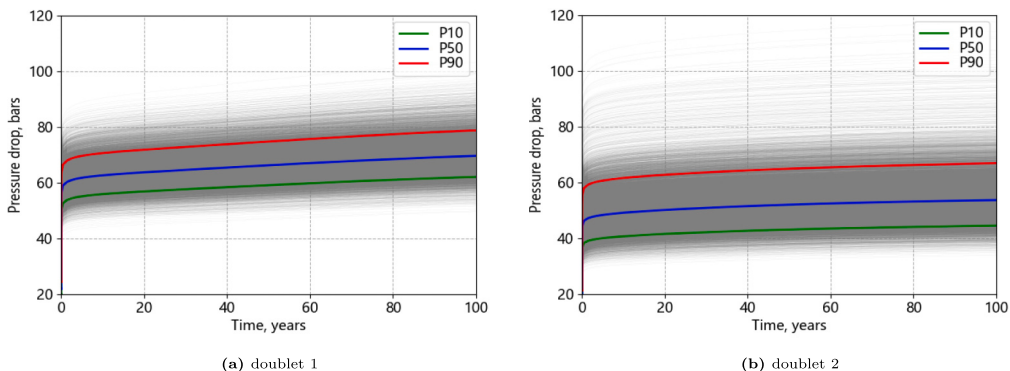


Fig. 9. Pressure drop within doublet 1 and 2, and the corresponding P10, P50, P90 of pressure drop.

Influenced by other input parameters and by the number of filtered realizations, the distribution of produced energy varies significantly within each subplot. However, the mean values of energy are not sensitive to individual parameters, except to the salinity. The energy

production is directly associated with the fluid density Eq. (10), which is the function of salinity Eq. (1). Therefore, the shift of the mean energy value to salinity is straightforward. The injectivity coefficient mainly influences the operating pressure difference within each doublet

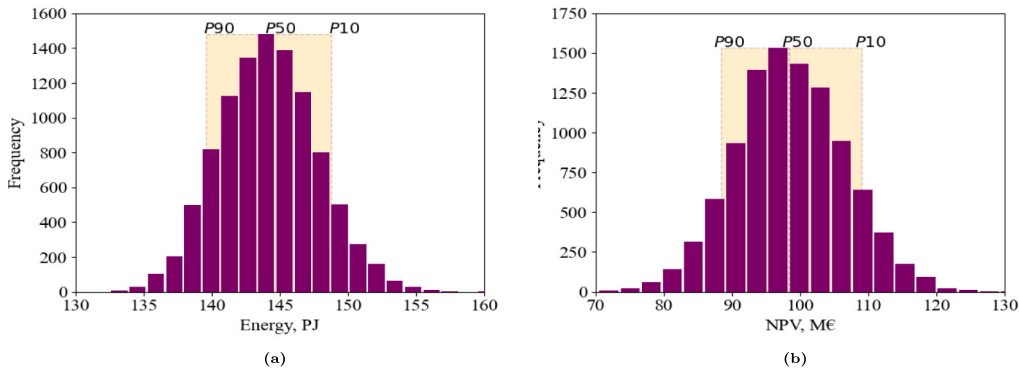


Fig. 10. The histograms of produced energy and NPV of the geothermal project. The samples falling between P10 and P90 quantiles of both parameters are marked in orange. (For interpretation of the references to color in this figure legend, the reader is referred to the web version of this article.)

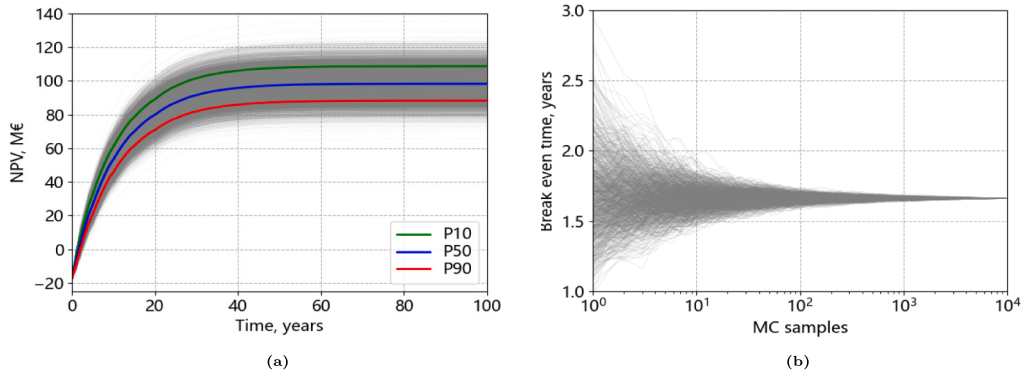


Fig. 11. (a) Cumulative NPV of all realizations along the simulation and P10, P50, P90 quantiles of NPV; (b) Break-even time of the project.

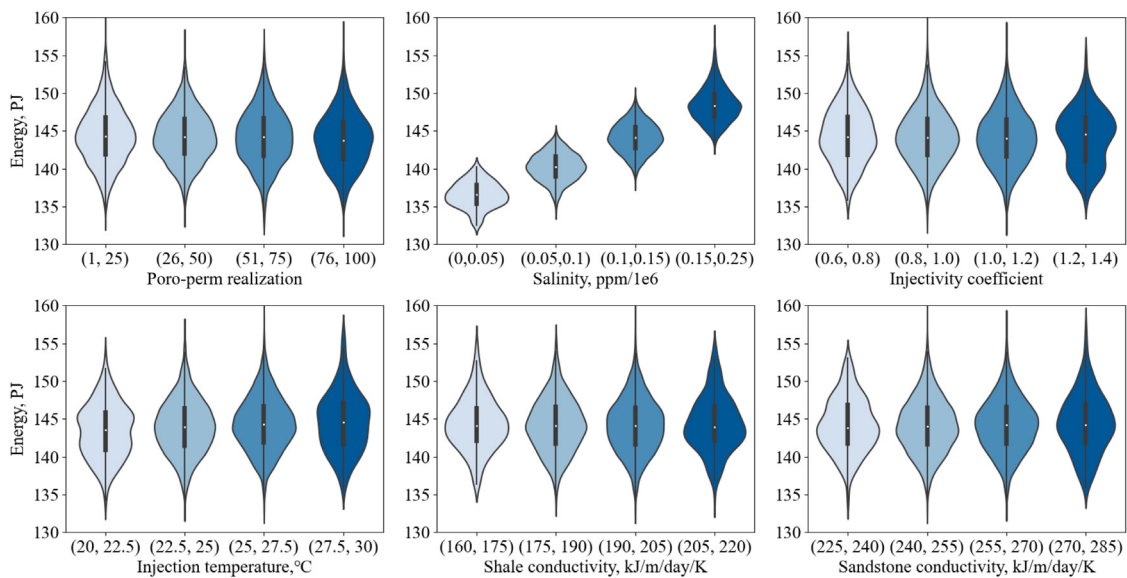


Fig. 12. The uncertainty of energy production to the individual uncertain input parameter.

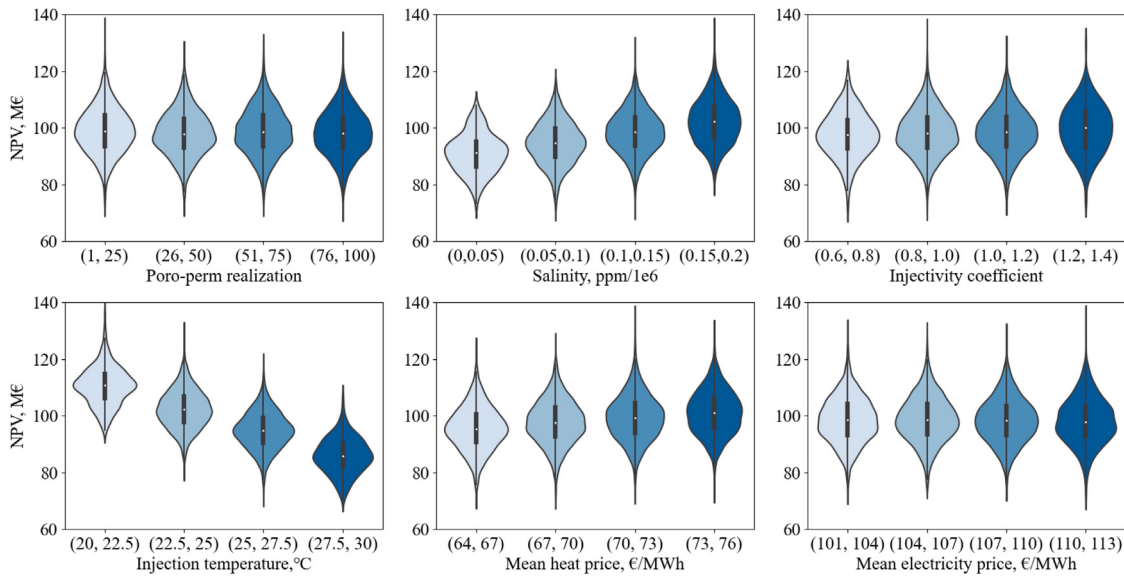


Fig. 13. The uncertainty of NPV to individual uncertain input parameter.

and the energy production is not visibly affected under the constant rate operation.

In fluvial systems, shale influences energy production via thermal conduction as an additional heat source. In our previous work with the same model (Wang et al., 2021), we analyzed the significant influence of shale on energy production by including and excluding the shale facies. In Fig. 12, the overall variation of produced energy to thermal conductivity is not obvious for the typical conductivity ranges used in this study.

Similarly, Fig. 13 displays the uncertainty of NPV to six parameters (poro-perm realization, salinity, injectivity coefficient, injection temperature, mean heat and electricity price). Note that since the heat and electricity prices fluctuate with time, their mean value during the total 100-years period is collected for each MC realization, composing the data set of mean prices. We can see a large uncertainty of mean NPV with the variation of salinity, injection temperature and mean heat price. This also explains the observation of larger uncertainty in NPV than in energy from the previous section. Since NPV is positively correlated with generated energy, it increases with salinity and similarly with heat price as well. The injection temperature influences NPV via the system power (Eq. (12)) as higher injection temperature causes lower system power and therefore, lower NPV. The electricity cost only takes a small portion of the total NPV calculation, which is verified by the short break-even time (in Fig. 11(b)) of this project.

4.4. The effect of upscaling

In this section, to check the cold plume propagation under different resolutions, the original model is upscaled to different levels of resolutions. The accuracy of the upscaled model highly depends on the upscaling factor and the proportion of the non-reservoir lithology (i.e., impermeable shale facies). The non-reservoir lithology will heavily impact the thermal propagation inside the reservoir via thermal conduction, whose evaluation highly depends on the model resolution. In other words, the loss of information during upscaling may lead to inaccurate simulation results.

Here, several upscaling methods (namely, arithmetic, geometric and harmonic averaging) for reservoir properties along the vertical direction were tested, where arithmetic averaging performs the best which is consistent with our earlier studies (Shetty et al., 2018; Perkins, 2019). The original model is with 895 vertical layers, which were then gradually upscaled to 101, 9 and 1 layers along the vertical direction.

Two out of the 100 realizations (porosity-permeability distributions) are randomly selected as the showcase for the original and upscaled models. Figs. 14 and 15 display the porosity, permeability, temperature fields and cold front plumes of the two selected realizations with different vertical upscaling factors. As is shown, the deviations of upscaled models to the original model in both reservoir properties (porosity and permeability) and simulation results (temperature field and cold front plume) enlarge with the upscaling factors.

Though with noticeable deviations in cold front propagation, the upscaled 2D models are commonly used to perform UQ analysis (Veldkamp et al., 2015) in place of detailed 3D geological models. Based on all the 100 realizations of the geological model used in this study, the corresponding 2D models have been generated through grid upscaling along the vertical direction. The amount of mass and energy in the system is ensured to conserve for each geological realization via volume-based upscaling. Moreover, the topography of the 3D model is preserved by upscaling the unique Corner Point Geometry (CPG) meshes of the original model. After upscaling, the original ~3.2 million grid blocks are reduced by ~200 times to ~15,000 grid blocks. With all upscaled 2D models, the same routine using MC simulation for UQ of 3D models is conducted. The simulation results are collected and plotted in Fig. 16.

Fig. 16(a) displays the production temperature of doublet 1 during an extended development period of 200 years since the temperature drop within the first 100 years is small. While the production temperature of doublet 2 is not shown here because it keeps as the initial value during the whole simulation period of 200 years. The production temperature of doublet 1 in the upscaled model shows a large difference from that in the 3D model (Fig. 8(a)). The cold front in the upscaled 2D model propagates much slower than in the 3D model. This is because the original 3D layering is represented by a single layer, which instantaneously equilibrates temperature in a vertical direction during the simulation. Therefore, the cold water plume in the 2D reservoir looks mitigated.

Fig. 16(b) shows the probability density function of total energy production during the simulation of the first 100 years. Compared with Fig. 10(a), the distribution is shifted towards the positive X direction. A larger P50 is observed on the energy histogram of the 2D model. Without an apparent drop in the production temperature of the 2D model in the first 100 years, the energy output stays stable as the initial energy production rate for each Monte Carlo sample. The distribution of produced energy follows closely the distribution of salinity, which

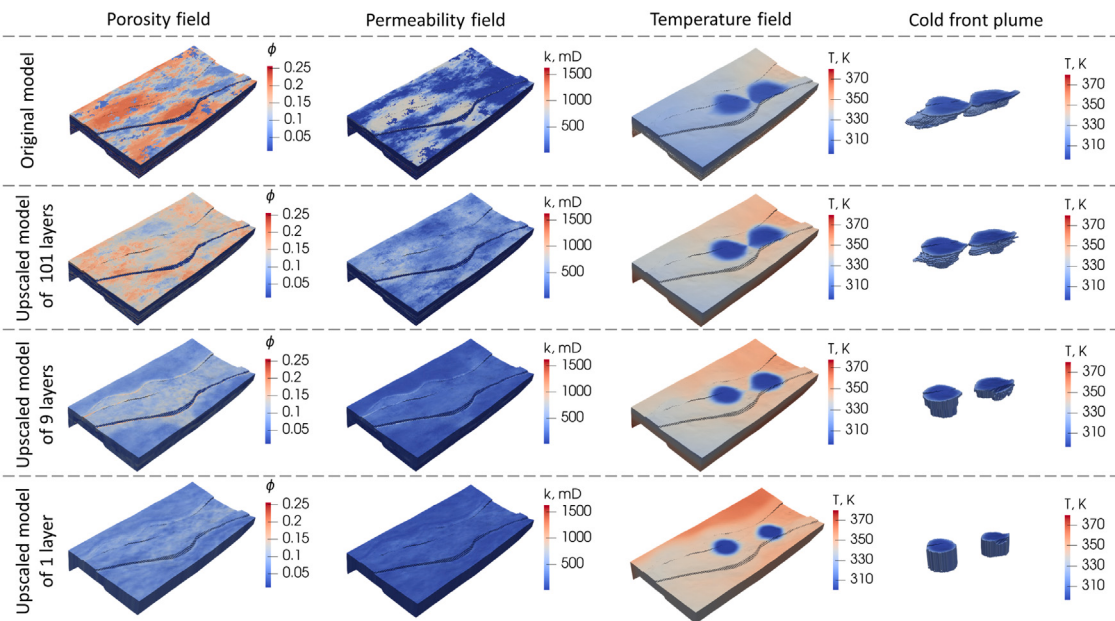


Fig. 14. The porosity, permeability, temperature fields and cold front plumes of one realization.

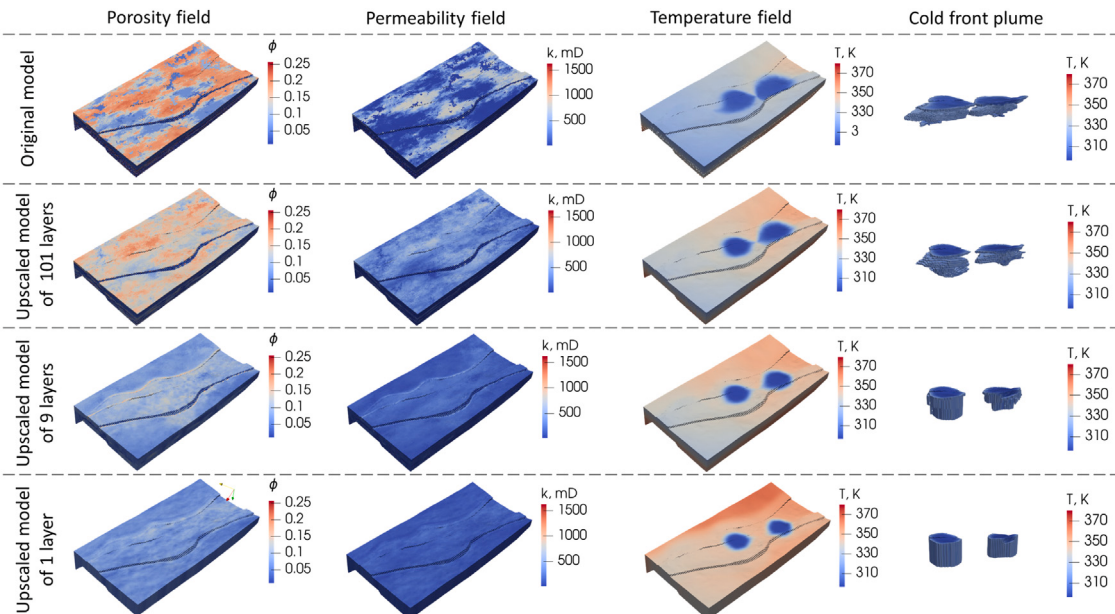


Fig. 15. The porosity, permeability, temperature fields and cold front plumes of another realization.

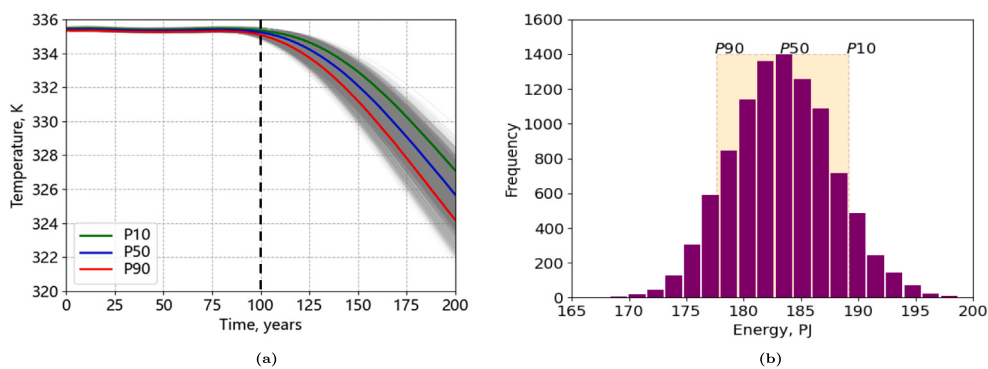


Fig. 16. (a) Production temperature of doublet 1 in the upscaled 2D model. (b) The histogram of produced energy of the upscaled 2D model. The samples falling between P10 and P90 quantiles are marked in orange. (For interpretation of the references to color in this figure legend, the reader is referred to the web version of this article.)

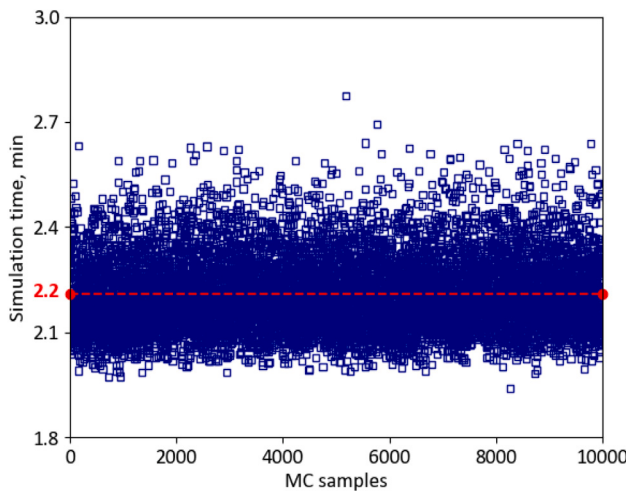


Fig. 17. A collection about the simulation time of all 3D realizations. The red dashed line marks the mean value of the simulation time.

is positively correlated with the amount of energy carried by the fluids. From this perspective, the impact of other uncertain parameters on energy production can hardly be detected. Through the comparisons above, the upscaled 2D model cannot accurately reproduce the production temperature and energy from the 3D model in the UQ.

4.5. Simulation time

Owing to the high computing performance of the GPU version of DARTS, the mean simulation time for a 100-years simulation (with a maximum timestep of one year) of the high-fidelity 3D model (with ~3.2 million grid cells) stabilizes at 2.2 min on the Titan RTX GPU card. The average numbers of nonlinear and linear iterations for the simulations are 117 and 922. The simulation cost is mainly occupied by the nonlinear and linear iterations, which on average take 19.8 and 74.4 s. The connection lists of the 100 geological realizations have been pre-generated. During the MC simulation, the connection lists are read in the simulator directly, which saves time for the pre-processing. According to Khait et al. (2020), the benchmarked simulation with the same model on a single thread CPU of Intel Core i7-8086K requires about 80 min to run for 100 years (or approximately 40 min for a 50-years simulation). The performance has been improved by more than an order of magnitude. Using the Monte Carlo method, it is convenient to run multiple simulations in parallel. This UQ study was performed on 16 GPU cards simultaneously. A total 10,000 simulations were finished within 23 h as shown in Fig. 17.

5. Discussion

From the porosity and permeability fields in Figs. 14 and 15, we can see the heterogeneity of the models reduces with the increase of upscaling factors for both realizations. During upscaling process, the reservoir properties are averaged along the vertical direction based on the upscaling intervals. The strong heterogeneity in the original model is gradually smeared during the lumping of grid blocks. For the extreme 2D case, there is only one upscaling interval which ultimately integrates all vertical layers into one layer. Therefore, the model becomes more homogenized with upscaling and loses the unique heterogeneous feature.

As for cold front propagation in Figs. 14 and 15, the swept area becomes narrower with the increase of upscaling factors from the observation of the temperature field. A more intuitional representation of cold front propagation is displayed in the 3D plumes, where the shape of the cold front is clearly delineated. Due to the strong heterogeneity

within the original model, the cold front propagates along the high-flow channels within the reservoir. Therefore, the 3D cold front plume is present in an irregular shape. As the model is upscaled, the shape of the plume becomes more regular and restricted, which delivers a clear explanation about why the outputs of an upscaled model distinguish from that of the original 3D model. First of all, this is partly because the reservoir properties among different vertical layers in the upscaled models become similar and the setup becomes more homogeneous with upscaling. Thereby, the difference in cold water propagation among upscaled vertical layers decreases and the shapes of the plume become more uniform in the upscaled setups.

In addition, the vertical upscaling lumps the sand and shale facies together. This replaces the original slower thermal conduction process with a vertical thermal equilibrium among layers, which will heavily impact thermal transportation. In the extreme 2D scenario, the vertical thermal equilibrium is achieved instantaneously. In the meanwhile, it is worth noticing that the amount of energy conserved within models under different resolutions. A vertical thermal equilibrium in the coarser setup means vertically-agglomerated energy will balance the temperature difference at the cold front. Therefore, the swept volume of the cold water within upscaled models shrinks with the same amount of injected cold water. With the analyses above, the mismatch in results between the original and upscaled models has been reasonably clarified.

To summarize, the upscaled setups will lose detailed heterogeneity information of the high-fidelity model, which will heavily impact the flow behavior of injected cold water within the reservoir. Besides, the vertical agglomeration of reservoir cells during upscaling will change the behavior of heat transport within the reservoir. It is not recommended to simulate the development of a geothermal reservoir with upscaled coarser models from the current investigation.

6. Conclusions

In this paper, systematic uncertainty quantification of a geothermal reservoir has been studied. The selected geothermal reservoir, located in the West Netherlands Basin, is thoroughly characterized with a “high-cell count” model to represent the detailed and inherent heterogeneity. The uncertain geological, physical, operational and economic parameters were incorporated into the investigation. With 3D high-resolution models, a large ensemble of 10,000 stochastic forward models has been simulated using a GPU version of DARTS to investigate the uncertain impacts of considered parameters.

After this, the 3D realizations were upscaled to a simplified upscaled 2D model. Using this model, the same uncertainty analyses were conducted and the simulation results between the upscaled 2D and fine-scale 3D models were compared. The high performance of the GPU version of DARTS and the paralleled feature of the Monte Carlo method guaranteed the large ensembles of forward simulations to be finished in an affordable time. The energy and NPV parameters were used as indicators for the convergence of MC simulations. After the convergence check, the uncertainties of energy and NPV were then discussed according to the numerical results.

Based on the analyses, the following conclusions can be drawn:

- A quick convergence of MC simulations has been achieved after 3000 simulations, which can be used as a reference number of MC simulations for future uncertain analyses.
- Larger uncertainty was present in NPV (21.21%) than in produced energy (6.25%), which is because more factors were encompassed in the NPV uncertainty evaluation.
- Salinity plays an important role in the uncertainty of both the produced energy and NPV. The value of salinity should be carefully evaluated based on field samplings or geological investigations in similar quantification of geothermal projects.

- Rock conductivity and injectivity coefficient are less influential to the uncertainty in system outputs, which indicates it is representative enough to use typical values.
- The attempt to replace the original 3D model with upscaled 2D models for UQ which is often performed in industrial studies (Veldkamp et al., 2015), failed and generated significant deviations in production temperature and energy. This demonstrates the simplification of physical processes and the loss of information during upscaling are detrimental to the accuracy of the prediction.
- High-fidelity 3D model is necessary to precisely capture the details of heterogeneity and thermal transport within the reservoir.

Through this study, we emphasized the importance of UQ to geothermal field development by demonstrating how various uncertain parameters affect the predictions of produced energy and NPV. The aggregated impact of all these parameters cannot be recognized without systematic UQ and ensembles of forward simulation. Also, the findings of this study can give an insight into the optimization of reservoir production under uncertainties.

CRediT authorship contribution statement

Yang Wang: Writing – original draft, Investigation. **Denis Voskov:** Supervision, Conceptualization, Methodology, Writing – review & editing. **Alexandros Daniilidis:** Conceptualization, Methodology, Software, Validation, Writing – review & editing, Visualization, Supervision. **Mark Khait:** Software. **Sanaz Saeid:** Methodology, Software, Formal analysis. **David Bruhn:** Supervision, Funding acquisition.

Declaration of competing interest

The authors declare that they have no known competing financial interests or personal relationships that could have appeared to influence the work reported in this paper.

Data availability

The data that has been used is confidential.

Acknowledgments

We acknowledge SURFSara for providing us access to their GPU cluster.

References

- Aliyu, M., Chen, H.-P., 2017. Sensitivity analysis of deep geothermal reservoir: Effect of reservoir parameters on production temperature. *Energy* 129, 101–113. <http://dx.doi.org/10.1016/j.energy.2017.04.091>.
- Athens, N., Caers, J., 2019. A Monte Carlo-based framework for assessing the value of information and development risk in geothermal exploration. *Appl. Energy* 256, 113932. <http://dx.doi.org/10.1016/j.apenergy.2019.113932>.
- Ballio, F., Guadagnini, A., 2004. Convergence assessment of numerical Monte Carlo simulations in groundwater hydrology. *Water Resour. Res.* 40 (4), W046031–W046035. <http://dx.doi.org/10.1029/2003WR002876>.
- Batzle, M., Wang, Z., 1992. Seismic properties of pore fluids. *Geophysics* 57 (11), 1396–1408. <http://dx.doi.org/10.1190/1.1443207>.
- Benson, S., Daggett, J., Iglesias, E., Arellano, V., Ortiz-Ramirez, J., 1987. Analysis of thermally induced permeability enhancement in geothermal injection wells. In: *Workshop on Geothermal Reservoir Engineering*.
- Bickel, J., Bratvold, R., 2008. From uncertainty quantification to decision making in the oil and gas industry. *Energy Explor. Exploit.* 26, 311–325. <http://dx.doi.org/10.1260/01445980878945344>.
- Borgia, A., Pruess, K., Kneafsey, T., Oldenburg, C., Pan, L., 2012. Numerical simulation of salt precipitation in the fractures of a CO₂-enhanced geothermal system. *Geothermics* 44, 13–22. <http://dx.doi.org/10.1016/j.geothermics.2012.06.002>.
- Chang, D., J., H., M., C., S., C., 1994. Effective porosity, producible fluid and permeability in carbonates from NMR logging. In: SPWLA 35th Annual Logging Symposium. URL <https://onepetro.org/SPWLAALS/proceedings-split/SPWLA-1994/SPWLA-1994-A/19156>.
- Chen, Y., Durlofsky, L., 2006. Adaptive local-global upscaling for general flow scenarios in heterogeneous formations. *Transp. Porous Media* 62, 157–185. <http://dx.doi.org/10.1007/s11242-005-0619-7>.
- Chen, Y., Durlofsky, L., Gerritsen, M., Wen, X., 2003. A coupled local-global upscaling approach for simulating flow in highly heterogeneous formations. *Adv. Water Resour.* 26 (10), 1041–1060. [http://dx.doi.org/10.1016/S0309-1708\(03\)00101-5](http://dx.doi.org/10.1016/S0309-1708(03)00101-5).
- Cremon, M., Christie, M., Gerritsen, M., 2020. Monte Carlo simulation for uncertainty quantification in reservoir simulation: A convergence study. *J. Pet. Sci. Eng.* 190, <http://dx.doi.org/10.1016/j.petrol.2020.107094>.
- Dai, Z., Viswanathan, H., Fessenden-Rahn, J., Middleton, R., Pan, F., Jia, W., Lee, S.-Y., McPherson, B., Ampomah, W., Grigg, R., 2014. Uncertainty quantification for CO₂ sequestration and enhanced oil recovery. 63, pp. 7685–7693. <http://dx.doi.org/10.1016/j.egypro.2014.11.802>.
- Daniilidis, A., Alpsoy, B., Herber, R., 2017. Impact of technical and economic uncertainties on the economic performance of a deep geothermal heat system. *Renew. Energy* 114, 805–816. <http://dx.doi.org/10.1016/j.renene.2017.07.090>.
- Daniilidis, A., Herber, R., 2017. Salt intrusions providing a new geothermal exploration target for higher energy recovery at shallower depths. *Energy* 118, 658–670. <http://dx.doi.org/10.1016/j.energy.2016.10.094>.
- Daniilidis, A., Nick, H., Bruhn, D., 2021. Interference between geothermal doublets across a fault under subsurface uncertainty; implications for field development and regulation. *Geothermics* 91, 1–13. <http://dx.doi.org/10.1016/j.geothermics.2021.102041>.
- DARTS, 2023. Delft advanced research terra simulator. URL <https://darts.citg.tudelft.nl>.
- De Paepe, M., Mertens, D., 2007. Combined heat and power in a liberalised energy market. *Energy Convers. Manage.* 48, 2542–2555. <http://dx.doi.org/10.1016/j.enconman.2007.03.019>.
- Gong, B., Karimi-Fard, M., Durlofsky, L., 2008. Upscaling discrete fracture characterizations to dual-porosity, dual-permeability models for efficient simulations of flow with strong gravitational effects. *SPE J.* 13 (1), 58–67. <http://dx.doi.org/10.2118/102491-pa>.
- James, A., Oldenburg, C., 1997. Linear and Monte Carlo uncertainty analysis for subsurface contaminant transport simulation. *Water Resour. Res.* 33 (11), 2495–2508. <http://dx.doi.org/10.1029/97WR01925>.
- Jansen, J., Douma, S., Brouwer, D., Van den Hof, P., Bosgra, O., Heemink, A., 2009. Closed-loop reservoir management. In: SPE Reservoir Simulation Symposium. <http://dx.doi.org/10.2118/119098-MS>.
- Kang, M., Jackson, R., 2016. Salinity of deep groundwater in California: Water quantity, quality, and protection. *Proc. Natl. Acad. Sci. USA* 113 (28), 7768–7773. <http://dx.doi.org/10.1073/pnas.1600400113>.
- Khait, M., Voskov, D., 2017. GPU-offloaded general purpose simulator for multiphase flow in porous media. In: SPE Reservoir Simulation Conference.
- Khait, M., Voskov, D., 2018. Operator-based linearization for efficient modeling of geothermal processes. *Geothermics* 74, 7–18. <http://dx.doi.org/10.1016/j.geothermics.2018.01.012>.
- Khait, M., Voskov, D., Zaydullin, R., 2020. High performance framework for modelling of complex subsurface flow and transport applications. In: 17th European Conference on the Mathematics of Oil Recovery. <http://dx.doi.org/10.3997/2214-4609.202035188>.
- Kretzschmar, H.J., Wagner, W., 2007. *International Steam Tables: Properties of Water and Steam Based on the Industrial Formulation IAPWS-IF97*. Springer Science & Business Media.
- Labus, M., Labus, K., 2018. Thermal conductivity and diffusivity of fine-grained sedimentary rocks. *J. Therm. Anal. Calorim.* 132, 1669–1676. <http://dx.doi.org/10.1007/s10973-018-7090-5>.
- Major, M., Daniilidis, A., Hansen, T., Khait, M., D., V., 2023. Influence of process-based, stochastic and deterministic methods for representing heterogeneity in fluvial geothermal systems. *Geothermics* 109, 102651. <http://dx.doi.org/10.1016/j.geothermics.2023.102651>.
- MidttØmme, K., Roaldset, E., 1999. Thermal conductivity of sedimentary rocks: uncertainties in measurement and modelling. *Geol. Soc. Special Publ.* 158, 45–60. <http://dx.doi.org/10.1144/GSL.SP.1999.158.01.04>.
- PanTerra Geoconsultants, 2018. Project Report: G1330c. Technical Report.
- Peaceman, D.W., 1983. Interpretation of well-block pressures in numerical reservoir simulation with nonsquare grid blocks and anisotropic permeability. *Soc. Petrol. Eng. J.* 23 (3), 531–543. <http://dx.doi.org/10.2118/10528-PA>.
- Perkins, D., 2019. Reservoir simulation for play-based development of low enthalpy geothermal resources. URL <https://repository.tudelft.nl>.
- Saeid, S., Al-Khoury, R., Nick, H., Hicks, M., 2015. A prototype design model for deep lowenthalpy hydrothermal systems. *Renew. Energy* 77, 408–422. <http://dx.doi.org/10.1016/j.renene.2014.12.018>.
- Saeid, S., Wang, Y., A., D., Khait, M., Voskov, D., Bruhn, D., 2020. Lifetime and energy prediction of geothermal systems: Uncertainty analysis in highly heterogeneous geothermal reservoirs (Netherlands). In: World Geothermal Congress. URL <https://pangea.stanford.edu/ERE/db/WGC/papers/WGC/2020/22157.pdf>.
- Scheidt, C., Caers, J., 2009. Uncertainty quantification in reservoir performance using distances and kernel methods-application to a west Africa deepwater turbidite reservoir. *SPE J.* 14 (4), 680–692. <http://dx.doi.org/10.2118/118740-PA>.

- Shetty, S., Voskov, D., Bruhn, D.F., 2018. Numerical strategy for uncertainty quantification in low enthalpy geothermal projects. In: Workshop on Geothermal Reservoir Engineering 2018. URL <https://pangea.stanford.edu/ERE/pdf/IGAstandard/SGW/2018/Shetty.pdf>.
- TNO, 2018. ThermoGIS v2.0 - economic model. URL <https://www.thermogis.nl/en/economic-model>.
- Veldkamp, J.G., Pluymaekers, M.P.D., van Wees, J.D.A.M., 2015. DoubletCalc 2d 1.0 user manual. Technical Report.
- Voskov, D., 2017. Operator-based linearization approach for modeling of multiphase multi-component flow in porous media. *J. Comput. Phys.* 337, 275–288. <http://dx.doi.org/10.1016/j.jcp.2017.02.041>.
- Wang, Y., Voskov, D., Khait, M., Bruhn, D., 2020. An efficient numerical simulator for geothermal simulation: A benchmark study. *Appl. Energy* 264, <http://dx.doi.org/10.1016/j.apenergy.2020.114693>.
- Wang, Y., Voskov, D., Khait, M., Saeid, S., Bruhn, D., 2021. Influential factors on the development of a low-enthalpy geothermal reservoir: a sensitivity study of a realistic field. *Renewable Energy* 179, 641–651. <http://dx.doi.org/10.1016/j.renene.2021.07.017>.
- Willems, C., Vondrak, A., Mijnlieff, H., Donselaar, M., van Kempen, B., 2020. Geology of the upper Jurassic to Lower Cretaceous geothermal aquifers in the West Netherlands Basin – an overview. *Neth. J. Geosci.* 99, 1–13. <http://dx.doi.org/10.1017/njg.2020.1>.
- Xu, T., Apps, J., Pruess, K., Yamamoto, H., 2007. Numerical modeling of injection and mineral trapping of CO₂ with H₂S and SO₂ in a sandstone formation. *Chem. Geol.* 242, 319–346. <http://dx.doi.org/10.1016/j.chemgeo.2007.03.022>.
- Zaal, C., Daniilidis, A., Vossepoel, F., 2021. Economic and fault stability analysis of geothermal field development in direct-use hydrothermal reservoirs. *Geotherm. Energy* 9, 1–26. <http://dx.doi.org/10.1186/s40517-021-00193-0>.